Active stress patterns orchestrate the organization of epithelial cell monolayers

Lakshmi Balasubramaniam,[1*] Amin Doostmohammadi,[2,3*¶]
Thuan Beng Saw,[4,5] Gautham Hari Narayana Sankara Narayana,[1]
Romain Mueller,[3] Tien Dang,[1] Shafali Gupta,[6] Surabhi Sonam,[1,7] Alpha S. Yap,[6]
René-Marc Mège,[1¶] Julia Yeomans,[3¶] Benoît Ladoux[1¶]

[1]Institut Jacques Monod (IJM), CNRS UMR 7592 et Université de Paris,
75013 Paris, France,
[2]Niels Bohr Institute, University of Copenhagen,
Blegdamsvej 17, 2100 Copenhagen, Denmark
[3]The Rudolf Peierls Centre for Theoretical Physics, University of Oxford,
Parks Road, Oxford OX1 3PU, UK
[4]Mechanobiology Institute (MBI), National University of Singapore, Singapore, 117411
[5] National University of Singapore, Department of Biomedical Engineering,
4 Engineering Drive 3, Engineering Block 4, # 04-08, Singapore, 117583
[6]Division of Cell and Developmental Biology, Institute for Molecular Bioscience,
The University of Queensland, St. Lucia, Brisbane, QLD 4072, Australia
[7]Present address: D Y Patil International University, Akurdi, Pune, India

*These authors contributed equally to this work

¶To whom correspondence should be addressed;
doostmohammadi@nbi.ku.dk, rene-marc.mege@ijm.fr
julia.yeomans@physics.ox.ac.uk, benoit.ladoux@ijm.fr

The actomyosin machinery endows cells with contractility. However, within a tissue, cells can show either contractile or extensile force patterns. How these

two contradictory mode of force generation can coexist remains unexplained. Here, using a combination of experiments and simulations, we uncover the mechanism behind the switch in behaviour of cell monolayers from extensile to contractile as the weakening of intercellular contacts. We find that this switch in active behaviour also promotes the buildup of tension at the cell-substrate interface and triggers a mechanotransduction response in vinculin translocation and YAP activation. Our studies show that differences in extensility and contractility act to sort cells, thus determining a general mechanism for mechanobiological pattern formation during cell competition, morphogenesis and cancer progression. 120/125

Main text

The ability of cell monolayers to self-organise, migrate and evolve depends crucially on the interplay between cell-matrix and cell-cell interactions (*1–6*) which controls various phenomena including tissue morphogenesis (*7*), epithelial-mesenchymal transition (*1*), wound healing and tumour progression (*8*). Cells are active systems, engines that operate away from thermal equilibrium, transducing chemical energy into motion. Single cells generate contractile force dipoles: The resultant of the forces due to actomyosin contraction, pulling on focal adhesions and substrate friction, is typically a pair of approximately equal and opposite forces acting inwards along the cellular long axis (*9*) (Figure 1A). It is reasonable to expect that contractile particles also generate contractile behaviour in the monolayer (*10*). However, at the collective cell level, epithelial monolayers display extensile behavior (*11*) i.e. net force from the neighbours and substrate interaction act to further elongate the cell further (Figure 1B inset). This immediately poses the question of how the crossover occurs as the emergence of such differences in active behaviour may be crucial in understanding biological processes such as tissue

homeostasis, cell competition and self organization (*12*).

The structure of flow fields around topological defects provide a way to determine the contractility or extensility within cell populations. Topological defects are singular points in the orientation field of the cell monolayers, where the orientation of a cell is defined as the direction of its long axis (see Methods). In a cellular monolayer two types of topological defects predominate: comet-shaped defects and trefoils (Figure 1C), which correspond to topological defects in nematic liquid crystals with charges +1/2 and -1/2, respectively (*10, 11, 13–15*).

Of relevance here in active systems, the active nature of cells results in a directed motion of the comet shaped defects. For extensile systems the defects move in the direction of the head of the comet (Figure 1B), while topological defects in contractile systems move towards the comet tail (Figure 1A). This is illustrated by measurements of the average flow field around the comet defects in Madine-Darby Canine Kidney (MDCK) monolayers using Particle Image Velocimetry (PIV). The results show clearly that the comet-shaped defects move in the tail-to-head direction (Figure 1D), indicating that at the collective level the MDCK monolayer behaves as an extensile active system despite forming contractile dipoles at a single cell level (Figure 1A). Similar behaviour has been recently reported for Human Bronchial Epithelial Cells (HBEC) (*15*). By contrast the flow field around comet defects in a monolayer of fibroblasts has an opposite flow direction - from head-to-tail of the comet - indicating that the fibroblast cells behave as contractile system at the collective level (Figure S1A), in agreement with previous studies (*10*). But what causes epithelial cells to behave as an extensile system at the collective level and mesenchymal cells as a contractile system?

One fundamental difference between epithelial and mesenchymal cells is the ability of epithelial cells to form strong cell-cell adhesions through E-cadherin based junctional complexes, responsible for active intercellular force transmission (*16*). We therefore asked if weakening this

intercellular adhesion in epithelial cells results in a (mesenchymal-like) contractile behaviour at the collective level. To test this, we inactivated the E-cadherin gene in MDCK cells using CRISPR-Cas9 which was validated through immunostaining and western blot analysis (Figure S2). E-cadherin Knock-Out (KO) MDCK cells can still maintain their contacts through another form of cadherin (cadherin 6) (*17*), albeit with a significantly weaker adhesion strength as observed through the reduced level of β-catenin at adherens junctions (Figure S2), while still being able to form tight junctions (Figure S2) at similar density. Strikingly, in these E-cadherin KO monolayers, the average flow field around comet defects switches direction compared to the Wild-Type (WT) cells, indicating a contractile behaviour at the collective level similar to that of fibroblasts (Figure 1D and E). Therefore, epithelial monolayers behave as an extensile system due to the presence of strong cell-cell adhesions and loosening this adhesion by removing E-cadherin results in a contractile behaviour. In order to check that this switch between extensile to contractile behaviour is not only specific to MDCK cells, we further validated the results by perturbing cell-cell contacts in the human breast cancer cell line MCF7A, where depleting E-cadherin by RNAi changed the behaviour from an extensile to a contractile system (Figure S3). This switch was not a clonal effect as rexpression of E-cadherin restored collective extensile behaviour to E-Cadherin KO MDCK cells. (Figure S4C).

We next checked whether the extensile to contractile crossover could be inferred from the behaviour of individual cells. From our traction force data, both single isolated WT and single isolated E-cadherin KO cells showed contractile behaviour with the forces directed inwards along their elongation axes as cells pulled on the substrate (Figure 1A and S4A). This indicates that removing E-cadherin does not change the contractility pattern of single cells. Therefore the change from contractile to extensile behaviour at the collective level can be linked to the presence of E-cadherin which mediates force transmission between neighbouring cells.

In order to better discern the competition between intracellular contractile stresses (generated by the actomyosin machinery throughout the cell) and the intercellular stresses (due to neighbour interactions), we employed a cell-based model which allows for these two stresses to vary independently. The model is based on a phase-field formulation (*18*) that captures the deformation of individual cells, and has recently been shown to reproduce the formation of topological defects in MDCK monolayers and their associated flow field and stress patterns (*19*) of an extensile system. In a similar manner as experimental analysis where the orientation of cells were identified through its long axis, in the model a shape tensor, S, characterises the magnitude and direction of cell elongation (Figure 2A). This parameter continuously evolves with deformation of cells as they push/pull on their neighbors within the monolayer. Following our recent work (*19*), intercellular stresses are defined to be proportional to the shape tensor which allows us to model extensile stresses at the cell-cell contacts (Figure 2A). This form of modeling was inspired by previous studies on adherens junctions and actomyosin interaction which showed that force transduction at the junction can modify the actomyosin network and in turn the cell shape (*20*). In addition, an intracellular stress is defined to mimic internal stresses generated by acto-myosin complexes within the individual cells (see Methods for the details of the model). The effect of E-cadherin removal is thus captured in the model by tuning down the intercellular stresses. Just as in the experiments both comet-shaped and trefoil topological defects (+1/2 and -1/2 charges, respectively) are found in the orientation field of the monolayer (Figure 2B) and the flow fields around topological defects match those measured for the WT cells (Figure 2C). More importantly, we found that lowering intercellular stresses resulted in the switching of the flow direction around comet-shaped topological defects in agreement with experimental results of E-cadherin KO (Figure 2B and C). Quantitative analysis of the simulations showed that reducing the intercellular stresses results in slower dynamics characterised by a smaller rms-velocity (Figure 3A) and generates less correlated patterns of motion characterised by a smaller

velocity correlation length (Figure 3B). Moreover, because of the dipolar symmetry of the intercellular stresses in the model, simulation results predict that the switching from extensile to contractile behaviour does not alter the isotropic stress patterns, i.e., tension (positive isotropic stress) and compression (negative isotropic stress) around the defects (Figure 3C).

To test the predictions of the model we first experimentally studied the effect of E-cadherin KO on the stress patterns around topological defects and on the collective motion of the cells. From the traction forces in the monolayer, we inferred the associated stress patterns using Bayesian Inversion Stress Microscopy (BISM) (*21*). Experiments agreed with the simulations in showing no difference in the isotropic stresses around comet defects between the WT and E-cadherin KO cells (Figure 3D) while they still show a difference in their velocity flow field (Figure S4B) (*11*), indicating that the tension and compression around defects are primarily controlled by local cellular organisation and elongation. Moreover, measuring the velocity correlation function (*22*), we found it to be consistent with the numerical predictions whereby removing E-cadherin reduces the correlation length compared to the WT cells (Figure 3E). This is also in agreement with previous reports which demonstrate a reduction in velocity correlation length of mesenchymal cells with respect to epithelial cells (*22*). Interestingly, by performing rescue experiments to put E-cadherin back, we found an increase in velocity correlation length (Figure 3E). This indicates that the perturbation of junctional protein E-cadherin can be used as an effective way of tuning the collective contractility and extensility of the epithelial monolayer.

Comparing the average velocities in the monolayers with and without E-cadherin also agreed with the model's prediction that cellular velocity is reduced upon E-cadherin depletion (Figure 3F) at similar density. Interestingly, traction force microscopy measurements revealed that this reduction in velocity is accompanied by a significant (about six fold) increase in the average

traction forces that cells in the monolayer exert on their underlying substrate (Figure 3G). Furthermore, comparing average cell areas in the WT and E-cadherin KO monolayers indicated an increase in spreading area of the cells within the monolayer (Figure 4A), while the aspect ratio of the cells remained unchanged (Figure 4B) at similar density. These measurements of velocity reduction, traction force increase, and area increase in the monolayers without E-cadherin, combined together, hinted that the cell-substrate interaction increased as the cell-cell interaction was weakened, indicating a possible cross-talk between the two interactions.

To examine this, and since the spreading capabilities of cells are associated with mechanosensory mechanisms at cell-matrix adhesions (*23, 24*), we asked if the increase in the average area of E-cadherin KO cells results in any change in their mechanotransductory response. Using actin staining we first checked for changes in the organisation of stress fibers in the cells within a monolayer, as stress fiber formation is an important determinant of force generation by cells on a substrate (*25, 26*). Indeed, comparing the actin configuration of WT and E-cadherin KO cells, we found a considerable increase in stress fibers in the absence of E-cadherin (Figure 4C). Concomitantly, phosphomyosin staining of WT and E-cadherin KO monolayers in our experiments showed an increase in the number of phospho myosin light chain (pMLC2) fibers (Figure 4C) generated at the basal surface within E-cadherin KO cells. Western blot analyses further revealed an increase in the total level of myosin light chains (MLC2) (Figure 4C). Considering these results we reasoned that inhibiting cell contractility in E-cadherin KO cells may alter their active behavior. Upon treatment with a mild dose of blebbistatin (5 μM), an inhibitor of Myosin II (Figure S5A) E-cadherin KO monolayers still behave as a contractile system. However, a higher dose (20 μM) of Blebbistatin (Figure S5B) or 25 μM of Y27632, an inhibitor of ROCK 1 and 2 (Figure S5C) resulted in a switch in behaviour from a contractile to that of an extensile system (Table1). As a control we showed that similar treatments did not affect the extensile behaviour of the WT monolayers (Table 1, Figure S5D and E). Thus removing

E-cadherin not only reduces the extensile intercellular stresses, it also increases the intrinsic contractility generated by the cells at the cell-substrate interface. Since focal adhesions (FAs) are known to be mechanosensors at cell-matrix interface (*27*), we further investigated the assembly of FAs in E-cadherin KO and WT monolayers. By using paxillin staining to determine changes in FAs, we showed a marked increase both in length, and area within the cells (Figure 4E) in the E-cadherin KO cell monolayers in comparison to the WT cell monolayers. More importantly, we found that the E-cadherin KO modified the localisation of vinculin to the cell-substrate level, which is known to respond and transmit force from both integrin and cadherin based adhesion complexes (*28, 29*). Hence we conclude that vinculin was mostly present at the cell-cell junctions in the case of WT cells, however in the E-cadherin KO cells it relocalised to the basal plane (Figure 4E). The differences in focal adhesion and vinculin localization indicate an increase in cell-substrate adhesion in the E-cadherin KO cells. Since yes-associated protein (YAP) transcriptional activity is known to modify cell mechanics, force development and FA strength (*30,31*), we investigated YAP localisation within E-cadherin KO cells. Interestingly, we found that YAP was predominantly localised to the cell nucleus in E-cadherin KO cells (Figure 4F), which corresponds to the active state of YAP. This is in agreement with previous studies that showed YAP activation in the absence of E-cadherin or in well spread cells (*23, 32, 33*). Summarising, our results show that removing E-cadherin leads to a larger cell area, enhances the formation of stress fibers, promotes YAP activation, and leads to a marked increase in the formation of focal adhesions and their linkage to the substrate in turn triggering a contractile behaviour.

Our force measurements together with acto-myosin activity and adhesion patterns establish that whether epithelial tissues are extensile or contractile at a collective level relies on the interplay between active stresses at cell-cell and cell-matrix interfaces. To further explore this crossover we plated cells on a soft substrate, recalling that cellular responses on soft substrates leads to

lower contractility and less stable focal adhesions (*34*). MDCK WT cells remained extensile regardless of substrate stiffness (Figure S6A), while E-cadherin KO cells switched from contractile to extensile behaviour on a soft substrate (around 2.3 kPa) (Figure S6B). Taken together, these experiments show that tuning cell-cell and cell-substrate adhesion can result in a switch between extensile and contractile behaviour of cell monolayers.

Based on this difference in contractile and extensile behaviour, we next used the model to produce testable predictions. We simulated the interaction between the extensile and contractile system, where we noticed that the two different domains were able to separate out into two different phases (Figure 4G) where extensile cells were surrounded by contractile ones. Similarly, we were able to replicate this experimentally (Figure 4H) where WT and E-cadherin KO cells separate out into two different phases with WT cells surrounded by E-cadherin KO cells when plated at a 50-50 ratio. Even though tissue segregation was first exemplified based on differences in cadherin-mediated surface tension (*35, 36*), it was later shown that intercellular adhesion is not the only mechanism that triggers cell sorting (*37*).Theoretical predictions have suggested that cell sorting could be driven by a combination of cell surface tension and contractility (*38*), although this has not been demonstrated experimentally. Our findings highlight the importance of active nematic behaviours at a collective level to understand tissue shape and organization, factors central to morphogenesis (*39–41*). As such, the adaptation of cellular systems from extensile to contractile behaviours might be a crucial mechanism by which a collective living system undergoes morphological changes (sorting or tissue organization) based on a transition from a cohesive to a less coordinated organisation. Such a transition relying on the cross-talk between cell-cell and cell-matrix interactions may provide a new mechanism to understand cell migration during development, wound healing, and collective cancer cell invasion.

Methods

Cell culture and reagents MDCK WT (ATCC CCL-34) cells, MCF7A cells (ATCC HTB-22), MDCK E-cadherin Knock-Out (KO) cells and shMCF7A E-cadherin KD cells were cultured in DMEM (containing Glutamax, High Glucose, and Pyruvate, Life Technologies) supplemented with 10% foetal bovine serum (Life Technologies) and 1% penicillin-streptomycin (Life Technologies) at 37°C with 5% CO_2. For cell migration experiments, cells were let to spread overnight before imaging so that the cells form a complete monolayer. Prior to imaging, normal culture media (DMEM) was changed to low glucose DMEM (containing Pyruvate, Life Technologies) in order to minimize cell division as cell divisions were known to generate extensile flow (*42*). For immunofluorescent stainings, cells were fixed with 4% paraformaldehyde (PFA), permeabilized with 0.5% Triton-X 100 for 5 minutes, blocked with 1% BSA/PBS for 1 hour, and incubated with primary antibody overnight at 4°C . The samples were then incubated with secondary antibody and Hoescht (Thermo Fisher)(1:10000) for 1 hour and mounted on Mowiol 4-88 (Sigma Aldrich C2081) before imaging. The primary antibodies used were directed against E-cadherin (24E10- Cell Signaling Technology; DECMA1- Sigma Aldrich) (1:100), cadherin 6(1:50) (*17*), paxillin (Y133- Abcam) (1:100), pMLC2 (Cell Signaling) (1:100), vinculin (kindly provided by Marina Glukhova) (1:2) (*43*), α-catenin (Sigma Aldrich)(1:100), β-catenin (BD Biosciences) (1:100), ZO1 (a generous gift from Sylvie Robin) (1:50), YAP (Santa Cruz Biotechnology) (1:100). Anti-mouse, anti-rat, and anti-rabbit secondary antibodies conjugated with Alexa (488 or 568)(used at 1:200 dilution), Alexa 647 (1:50) conjugated phalloidin were purchased from Life Technologies. A slightly different fixation protocol was used to stain vinculin at the cell-cell junction and focal adhesion sites. In order to label vinculin at cell-cell contact sites, cells were fixed with a mix of 4% PFA and 0.5% Triton-X 100 for 1 minute 30sec, followed by fixation with 4% PFA for 10 minutes. While looking at vin-

culin at the focal adhesion sites, cells were fixed with 4% PFA for 10 minutes, followed by premeabilization with 0.5% Triton-X 100 for 10minutes. For experiments requiring inhibition of contractility blebbistatin $5\,\mu$M, $20\,\mu$M (Sigma Aldrich) or Y27632 $25\,\mu$M (Sigma Aldrich) were added 1 hour before imaging.

Generation of E-cadherin KO cell line MDCK E-cadherin KO stable cells were generated using a CRISPR-Cas9 double nickase plasmid (Santa Cruz Biotechnology). The following gRNA sequences were used: TGATGACACCCGATTCAAAG and ATAGGCTGTCCTAGGTAGAC. Around 2 million cells were electroporated (Neon Transfection System Invitrogen) with 3µg of plasmid in one pulse of 20 ms and at 1650V. Twenty four hours later, cells were selected by adding 2.5 µg/ml puromycin in the culture media. Fourty eight hours later, GFP positive single cells were sorted in 96 well plates by flow cytometry using Influx 500 sorter-analyzer (BD BioSciences). The clonal populations were then selected based on the absence of E-cadherin by immunofluorescence staining.The absence of E-cadherin in the clones generated was confirmed by Western blot analysis of protein extracts.

Generation of siRNA E-cadherin KD cells Lipofectamine RNAiMAX (Invitrogen) was used for siRNA transfection. siRNA sequences were control (on-target plus nontargeting pool), UGGUUUACAUGUCGACUAA. siRNA against E-cadherin : GGGACAACGUUUAUUACUA was used. The levels of E-cadherin was confirmed by Western blot analysis of protein extracts.

Live cell and fixed sample imaging Live imaging was performed with a 10X objective on BioStation IM-Q (Nikon) at 37°C and 5% CO2. Images are acquired every 10 min. For migration experiments, just the phase contrast images were captured every 10 min. For TFM experiments, phase contrast and fluorescent beads were imaged.

Calculation of cell area, aspect ratio and molecular markers The cellular area and aspect ratio were calculated manually from fixed images stained for junctional markers. The area and length of paxillin was obtained by fitting them with an ellipse. Nuclear-cytoplasmic ratio of YAP intensity was quantified using an in-house ImageJ script. If the nucleus-cytoplasmic ratio was greater than 1.1 then YAP was considered to be nuclear while a value less than 0.99 was considered to be more cytoplasmic while any value in between was considered to be uniformly distributed through the cell.

Western Blot Proteins for MDCK cells were extracted using RIPA buffer without SDS (50mM Tris pH 7.5, 150mM NaCl, 1% NP40, 5mM EDTA, 1mM Na3VO4, 10mM NaF, 1mM PMSF, 1X protease inhibitor cocktail (Roche) and 1X phosphatase inhibitor (Phosphostop, Roche).Proteins from MCF7 cells were extracted using sample buffer (50mM Tris pH 7.5, SDS 2%, Glycerol 10%, Bromophenol blue 0.1%, Dithiothreitol 400nM, sterile water). Protein concentration was quantified by a Bradford assay (BioRad). 30 µg of protein were loaded onto NuPage 4-12% Bis-Tris gel using a mini gel tank and dry transferred using iBlot transfer system (Invitrogen). Non-specific sites were blocked using 5% non fat dry milk in 0.1% PBS Tween. For pMLC and MLC total, blots were blocked with BSA/TBST (Tris buffered saline with Tween 20). Primary antibodies were diluted in PBS Tween at E-cadherin (24E10- 1:1000 for MDCK cells) (Santa Cruz, SC7870- 1:200 for MCF7 cells), α-catenin (1:1000), β-catenin (1:1000), GAPDH (Protein Tech Europe 60004-1 for MDCK cells and abcam- 1:5000, ab181603 for MCF7 cells- 1:500), alpha-tubulin (1:5000) (Sigma T9026) overnight on a shaker at 4 $^{\circ}$C. Anti-MLC (Cell Signaling) antibodies were diluted in TBST. The blots were then washed 3-4 times for 10minutes each in PBS 0.1% Tween or TBST (for pMLC2 and MLC total antibodies). They were then incubated with either Gampox, HRP linked (Sigma Aldrich, Pierce or Santa Cruz) or Dylight 800 linked secondary antibodies (ThermoFisher Scientific) for 2 hours. The blots were then

washed three times with PBS 0.1% Tween or TBST for 10 minutes each. The blots were then revealed using CHEMIDOC MP (BioRad) using Super West Femto (34095 Thermo Scientific) or chemiluminescence.

Traction force microscopy Soft silicone substrates were prepared as described previously (*44*). CyA and CyB were mixed in the ratio 1:1 and directly poured on glass bottom Petri dishes (fluorodish) in order to obtain a 100 µm thick layer. The substrate was cured at room temperature overnight on a flat surface. To ensure complete curing, the samples were cured at 80C for 1 hour the next day. The surface was silanized using a solution of 5% APTES diluted in absolute ethanol for 5 min. The substrate was then washed with absolute ethanol and dried at 80°C for 10 min. 200 nm carboxylated fluorescent beads (Invitrogen) were diluted in deionized water solution at 1:500 for 10 min, washed with deionized water and dried at 80°C for 10 min. We then coated these substrates with 50ug/ml fibronectin for 1 hour and washed with PBS prior to cell seeding. Around 200,000 cells were seeded in each petridish 40-50 min and washed with media when enough cells have attached. The cells were let to attach and spread overnight. The cells are imaged for 24 hours and at the end of the experiment, cells were removed with the addition of 500 µL of 10% SDS in the media so that the resting position of beads can be obtained.

Soft polyacrylamide gel patterning Glass coverslips were plasma activated and coated with 0.1mg/ml PLL-g-PEG (SuSoS Technology). 1mm diameter circles were patterned on the passivated glass coverslips using deep UV and incubated the glass coverslips with 20 µg/ml fibronectin for 30 minutes. After incubation, glass coverslips were rinsed in 1x PBS to remove excess protein. Simultaneously, silanization of another set of glass coverslips were performed by plasma activation of clean coverslips followed by incubation with an ethanol solution containing 2% (v/v) 3-(trimethoxysilyl) propyl methacrylate (Sigma-Aldrich, St Louis, Missouri,

USA) and 1% (v/v) acetic acid. The silanised coverslips were heated at 120°C. Freshly made polyacrylamide (PA) mix (7.5% acrylamide, 0.075% bis-acrylamide, 0.05% ammonium persulphate and 0.75 µl TEMED) was sandwiched between the patterned glass coverslip and silanized coverslip. The acrylamide, bis-acrylamide concentration was the same as (*45*), to generate 2.3kPa PA gels. After polymerization, the patterned coverslips were peeled off to reveal the patterns of protein on PA gels. Samples were kept submerged in 1x PBS until cell seeding.

Analysis methods Nematic analysis: Orientation field and defects were detected as described previously (*11*). In short, the largest eigen vector of the structure tensor was obtained for each pixel while the orientation of cells were obtained using a plugin on ImageJ called OrientationJ. Using the winding number parameter, we identify defects within the monolayer. Then we obtain the local nematic order parameter tensor Q (which is averaged over a region of 3-4 cells). The largest eigen vector of Q was taken to be the orientation of 3-5 cells and plotted as red lines over the phase image to ensure that orientation identified is correct. Using this Q value automated defect detection can be done using the winding number parameter thereby detecting the various defects (+1/2, -1/2, +1 and -1) although we have more +1/2 or -1/2 defects. In order to reduce noise, only stable defects which are found in at least six consecutive frames (60 mins) are used in the following analysis as described in (*11*).

Velocity analysis: We use PIVlab (a tool implemented using Matlab) to analyse the velocity of cellular monolayers. An interrogation window of 64x64 (40.96 µm) and 32x32 pixels (20.48 µm) with an overlap of 50% were used for this analysis. Outlier vectors were manually removed and a local standard deviation filter was applied. The velocity correlation length was obtained using the formula as detailed in (*22*).

Strain rate and stress measurement: Having identified the location of defects, we obtain the velocity field around the defects idetified by aligning these defects. The strain rate was calculated

from the gradient of velocity field as $\dot{\varepsilon} = \nabla \mathbf{v}$. By plotting the strain rate and velocity around the defect, we can characterize the system as an extensile or contractile system. For force measurement, the beads images obtained during cell migration are merged with the reference bead obtained after SDS treatment. The images are stabilized using the Image Stabilizer plugin in ImageJ after which the illumination is corrected to remove background noise. We then obtain the displacement of beads using PIV of interrogation window 32x32 pixel with an overlap of 50%. Using the ImageJ plugin FTTC (*46*) we correlate the bead displacement to traction forces using a regularization parameter of 9×10^{-9}. Stress within the monolayer was estimated using Bayesian Inversion Stress Microscopy (BISM) with a regularisation parameter of $\Lambda = 10^{-6}$. This method obtains the stress directly from traction forces irrespective of epithelial rheology. Isotropic stress was obtained as half the trace of the stress tensor (sxx+syy/2) in the tissue. Since the stress values obtained through this method are not reliable very close to the boundary, only defects in the center of the monoloyer have been taken into account in these calculations. The heatmaps obtained for strain rate and stress were smoothed through linear interpolation.

Statistics Differences between data were assessed using unpaired t-test implemented in Matlab and further verified using Graphpad Prism. On the plots, n.s.: not significant, $*p < 0.05$, $**p < 0.01$, $***p < 0.001$ and $***p < 0.0001$.

Computational model The model used in this manuscript is the extension of a recently developed phase-field model that has been shown to reproduce active nematic behavior in cellular tissues (*19*) and has been quantitatively compared with experiments of coherent oscillations in confined epithelial monolayers (*47*). We consider a two-dimensional tissue and describe each cell i independently by a phase-field ϕ_i, where $\phi_i \simeq 1$ indicates the interior of the cell and $\phi_i \simeq 0$ its exterior. The interface of each cell is thus lies at $\phi_i = 1/2$. The phase-fields dynam-

ics is given by a Cahn-Allen type evolution equation:

$$\partial_t \phi_i + \mathbf{v}_i \cdot \nabla \phi_i = -\frac{\delta \mathcal{F}}{\delta \phi_i}\,, \tag{1}$$

where $\mathbf{v}_i$ is the cell velocity that is determined from an over-damped equation for force balance as detailed below. $\mathcal{F}$ is the free energy that determines both mechanical properties of the cell - including cell stiffness and compressibility - and details of the passive interactions between the cells. As such the free energy $\mathcal{F} = \mathcal{F}_{\text{G-L}} + \mathcal{F}_{\text{area}} + \mathcal{F}_{\text{rep}}$ is composed of (i) Ginsburgh-Landau term $\mathcal{F}_{\text{G-L}}$, that stabilises the interface, (ii) a soft constraint for area conservation $\mathcal{F}_{\text{area}}$, that penalises deviations from an initial circular morphology of the cell, and (iii) $\mathcal{F}_{\text{rep}}$, which prevents two phase-fields from overlapping:

$$\begin{aligned}
F_{\text{G-L}} &= \sum_i \int \mathrm{d}\mathbf{x}\, \gamma \left\{ \frac{30}{\lambda^2}\, \phi_i^2 (1-\phi_i)^2 + (\nabla \phi_i)^2 \right\}, \\
F_{\text{area}} &= \sum_i \frac{\mu}{\pi R^2} \left(\pi R^2 - \int \mathrm{d}\mathbf{x}\, \phi_i^2 \right)^2, \\
F_{\text{rep}} &= \sum_i \sum_{j \neq i} \frac{30\kappa}{\lambda^2} \int \mathrm{d}\mathbf{x}\, \phi_i^2 \phi_j^2,
\end{aligned}$$

where λ sets the interface width, γ sets the stiffness, μ determines cells compressibility, and κ sets the strength of repulsion between two phase-fields. For the details of these free energy definitions, the reader is referred to recent reviews of phase-field models (*48, 49*) and to (*19, 47, 50, 51*) for recent implementations. Note that because here we model highly-packed, confluent tissues we do not introduce any thermodynamic attraction between the cells.

Force balance. We consider over-damped dynamics of cells moving on a substrate:

$$\xi \mathbf{v}_i = \vec{F}_i^{\text{tot}}, \tag{2}$$

where ξ is the friction coefficient between the cells and the substrate, and $\vec{F}_i^{\text{tot}}$ denotes the total forces acting on each cell, which encompasses self-propulsion forces generated by the cell

$\vec{F}_i^{\text{sp}}$ and the interaction forces $\vec{F}_i^{\text{int}}$ that a cell experiences from the neighbouring cells in the monolayer.

The self-propulsion force of an individual cell is achieved through an intricate coordination of actin polymerisation and myosin contractility. First, actin polymerisation at the cell front results in the formation of (lamelipodium) protrusions that deform the cell. Myosin contractility then retracts the cell rear to propel the cell forward. To account for the protrusion effects we introduce a polarity force $\alpha\vec{p}(i)$, that is distributed to the front edge of the cell in the direction of the cell polarity $\vec{p}_i$, where α sets the strengths of the polarity force. To account for the cell contractiltiy, we then introduce a contractile stress $\zeta_c \mathrm{Q}_i$, where ζ_c is the strength of the contractility and $\mathrm{Q}_i = \mathbf{p}_i^{\mathrm{T}}\mathbf{p}_i - \frac{\mathbb{I}}{2}\mathbf{p}_i^2$ is the tensor that characterises the orientation of the polarity: the largest eigenvector of Q_i is $\vec{p}_i$ meaning that the contractile stress acts along the direction of protrusions formation. Considering that the vectors $\nabla\phi_i$ describe the normal vector to the interface we obtain the following expression for the self-propulsion force:

$$\vec{F}_i^{\text{sp}} = \alpha\mathbf{p}_i + \int \mathrm{d}\mathbf{x} \left(\zeta_c \sum_j \phi_j \mathrm{Q}_j\right)\nabla\phi_i, \tag{3}$$

where matrix multiplication is implied in the last term.

Next we consider the interaction stresses σ_i^{int} to define the interaction forces $\vec{F}_i^{\text{int}} = \int \mathrm{d}\mathbf{x}\, \phi_i \vec{\nabla}\cdot\sigma^{\text{int}} = -\int \mathrm{d}\mathbf{x}\, \sigma^{\text{int}}\cdot\nabla\phi_i$. Note that $\vec{\nabla}\phi$ is only non-zero at the interfaces between the cells and as such the interaction force is acting at the cell-cell interfaces. We decompose the interaction stress in between the cells into passive and active contributions $\sigma_i^{\text{int}} = \sigma_i^{\text{passive}} + \sigma_i^{\text{active}}$: the passive contribution has a thermodynamic nature and is calculated from the free-energy:

$$\sigma_i^{\text{passive}} = \sum_i -\frac{\delta\mathcal{F}}{\delta\phi_i} \tag{4}$$

while the active contribution leads to the force generation between cells at their interface through

adherens junction. Following our recent work (*19*) this takes the form

$$\sigma_i^{\text{active}} = \zeta_s \sum_j \phi_j \mathrm{S}_j, \tag{5}$$

where $\mathrm{S}_i = -\int \mathrm{d}\mathbf{x}\, (\vec{\nabla}\phi_i)^{\mathrm{T}} \vec{\nabla}\phi_i$ is the deformation tensor for cell i, characterising the anisotropy of the cell shape such that the largest eigenvector of S_i corresponds to the direction of the elongation of the cell.

Alignment dynamics. We now introduce the dynamics of the cell polarity, modeling the mechanism that determines which direction the polar force should act on. There are many ways to introduce a dynamics of the polarisation (*52*). One such way is through modeling the phenomenon of "contact inhibition of locomotion (CIL)", aligning the polarity of the cell to the direction of the total interaction force acting on the cell: We define the dynamics of the polarisation to be given by

$$\partial_t \theta_i = -J |\vec{F}_i^{\text{int}}| \Delta\theta_i + D_r\, \eta, \tag{6}$$

where $\theta_i \in [-\pi, \pi]$ is the angle that the polarity vector is pointing at – such that $\vec{p}_i = (\cos\theta_i, \sin\theta_i)$ – and η is a Gaussian white noise with zero mean, unit variance, and the rotational diffusivity D_r. The positive constant J sets the time scale for the alignment of the polarity to the total interaction force, as was suggested theoretically (*53*) and has been recently confirmed in the experiments on epithelial cells (*47*). As explained in (*47*) this model of alignment has the advantage that (i) it contains an explicit timescale and (ii) does not require that a cell 'knows' about the position of its neighbours.

Simulation details We simulated equation (1) using a finite difference scheme on a square lattice with a predictor-corrector step. Throughout this article, we used the following numerical values for the simulation parameters: $\lambda = R = 8$, $\gamma = 0.02$, $\mu = 0.4$, $\kappa = 0.2$, $\xi = 1$, $\alpha = 0.2$,

$\zeta_c = 0.02$, and $\zeta_s = -0.02$. We simulated square domains of edge length $W = 100, 200, 400$ lattice sites with a packing fraction of $\Phi = 1.2$ cells and set $D_r = 1 \times 10^{-6}$ and $J = 0.02$.

Acknowledgements

This work was supported by the European Research Council (Grant No. CoG-617233), LABEX Who Am I? (ANR-11-LABX-0071), the Ligue Contre le Cancer (Equipe labellisée), and the Agence Nationale de la Recherche ('POLCAM' (ANR-17-CE13-0013 and 'MechanoAdipo' ANR-17-CE13-0012). We acknowledge the ImagoSeine core facility of the IJM, member of IBiSA and France-BioImaging (ANR-10-INBS-04) infrastructures. LB has received funding from the European Union's Horizon 2020 research and innovation programme (Marie Sklodowska-Curie grant agreement 665850-INSPIRE). T.B.S. acknowledges support from the Lee Kuan Yew (LKY) Postdoctoral fellowship and Singapore Ministry of Education Academic Research Fund Tier 1. S.G and A. Y were supported by project grants and fellowships from the National Health and Medical Research Council of Australia (1123816 and 1139592) and Australian Research Council (DP190102871). We would like to thank Phillipe Marcq for help with implementation of BISM code, Marina A. Glukhova for providing the vinculin antibody and Sylvie Robine for the ZO1 antibody. We also thank the members of cell adhesion and mechanics team at Institut Jacques Monod, Matthieu Piel and Francois Gallet for insightful discussions.

References

1. E. H. Barriga, K. Franze, G. Charras, R. Mayor, *Nature* **554**, 523 (2018).

2. E. Avizienyte, *et al.*, *Nature Cell Biology* **4**, 632 (2002).

3. T. Onodera, *et al.*, *Science* **329**, 562 (2010).

4. X. L. Chen, *et al.*, *Developmental Cell* **22**, 146 (2012).

5. W.-h. Guo, M. T. Frey, N. A. Burnham, Y.-l. Wang, *Biophysical Journal* **90**, 2213 (2006).

6. C. Malinverno, *et al.*, *Nature Materials* **16**, 587 (2017).

7. M. Cetera, *et al.*, *Nature Communications* **5**, 5511 (2014).

8. C. De Pascalis, S. Etienne-Manneville, *Molecular Biology of the Cell* **28**, 1833 (2017).

9. U. S. Schwarz, S. A. Safran, *Physical Review Letters* **88**, 048102 (2002).

10. G. Duclos, C. Erlenkämper, J.-F. Joanny, P. Silberzan, *Nature Physics* **13**, 58 (2017).

11. T. B. Saw, *et al.*, *Nature* **544**, 212 (2017).

12. W. Xi, T. B. Saw, D. Delacour, C. T. Lim, B. Ladoux, *Nature Reviews Materials* **4**, 23 (2019).

13. H. Gruler, U. Dewald, M. Eberhardt, *The European Physical Journal B* p. 6.

14. K. Kawaguchi, R. Kageyama, M. Sano, *Nature* **545**, 327 (2017).

15. C. Blanch-Mercader, *et al.*, *Physical Review Letters* **120**, 208101 (2018).

16. B. Ladoux, R.-M. Mège, *Nature Reviews Molecular Cell Biology* **18**, 743 (2017).

17. V. Marthiens, F. Padilla, M. Lambert, R. M. Mege, *Molecular and Cellular Neuroscience* **20**, 458 (2002).

18. W. Marth, A. Voigt, *Journal of Mathematical Biology* **69**, 91 (2014).

19. R. Mueller, J. M. Yeomans, A. Doostmohammadi, *Physical Review Letters* **122**, 048004 (2019).

20. M. R. Ng, A. Besser, J. S. Brugge, G. Danuser, *eLife* **3**, e03282 (2014).

21. V. Nier, *et al.*, *Biophysical Journal* **110**, 1625 (2016).

22. L. Petitjean, *et al.*, *Biophysical Journal* **98**, 1790 (2010).

23. S. Dupont, *et al.*, *Nature* **474**, 179 (2011).

24. G. Giannone, *et al.*, *Cell* **116**, 431 (2004).

25. A. Zemel, F. Rehfeldt, A. E. X. Brown, D. E. Discher, S. A. Safran, *Nature Physics* **6**, 468 (2010).

26. M. Gupta, *et al.*, *Nature Communications* **6**, 7525 (2015).

27. D. Riveline, *et al.*, *The Journal of Cell Biology* **153**, 1175 (2001).

28. S. Yonemura, Y. Wada, T. Watanabe, A. Nagafuchi, M. Shibata, *Nature Cell Biology* **12**, 533 (2010).

29. J. L. Bays, K. A. DeMali, *Cellular and Molecular Life Sciences* **74**, 2999 (2017).

30. G. Halder, S. Dupont, S. Piccolo, *Nature Reviews Molecular Cell Biology* **13**, 591 (2012).

31. G. Nardone, *et al.*, *Nature Communications* **8**, 15321 (2017).

32. B. W. Benham-Pyle, B. L. Pruitt, W. J. Nelson, *Science (New York, N.Y.)* **348**, 1024 (2015).

33. N.-G. Kim, E. Koh, X. Chen, B. M. Gumbiner, *Proceedings of the National Academy of Sciences* **108**, 11930 (2011).

34. D. E. Discher, P. Janmey, Y.-l. Wang, *Science* **310**, 1139 (2005).

35. W. A. Thomas, J. Thomson, J. L. Magnani, M. S. Steinberg, *Developmental Biology* **81**, 379 (1981).

36. J.-L. Maître, *et al.*, *Science* **338**, 253 (2012).

37. C. M. Niessen, B. M. Gumbiner, *The Journal of Cell Biology* **156**, 389 (2002).

38. M. L. Manning, R. A. Foty, M. S. Steinberg, E.-M. Schoetz, *Proceedings of the National Academy of Sciences* **107**, 12517 (2010).

39. B. Aigouy, *et al.*, *Cell* **142**, 773 (2010).

40. B. He, K. Doubrovinski, O. Polyakov, E. Wieschaus, *Nature* **508**, 392 (2014).

41. E. Hannezo, J. Prost, J.-F. Joanny, *Proceedings of the National Academy of Sciences* **111**, 27 (2014).

42. A. Doostmohammadi, *et al.*, *Soft Matter* **11**, 7328 (2015).

43. M. A. Glukhova, M. G. Frid, V. E. Koteliansky, *Journal of Biological Chemistry* **265**, 13042 (1990).

44. S. R. K. Vedula, *et al.*, *Nature Materials* **13**, 87 (2014).

45. S. V. Plotnikov, B. Sabass, U. S. Schwarz, C. M. Waterman, *Methods in cell biology* **123**, 367 (2014).

46. Q. Tseng, *et al.*, *Proceedings of the National Academy of Sciences* **109**, 1506 (2012).

47. G. Peyret, *et al.*, *Biophysical Journal* **117**, 464 (2019).

48. I. S. Aronson, ed., *Physical Models of Cell Motility*, Biological and Medical Physics, Biomedical Engineering (Springer International Publishing, 2016).

49. B. A. Camley, W.-J. Rappel, *Journal of Physics D: Applied Physics* **50** (2017).

50. B. Palmieri, Y. Bresler, D. Wirtz, M. Grant, *Scientific Reports* **5**, 11745 (2015).

51. B. Winkler, I. S. Aranson, F. Ziebert, *Communications Physics* **2**, 1 (2019).

52. R. Alert, X. Trepat (2019).

53. B. Smeets, *et al.*, *Proceedings of the National Academy of Sciences* **113**, 14621 (2016).

Figure 1| Active nematic behaviour of epithelial cellular systems change from extensile to contractile in the absence of E-cadherin. A) Top, left and right, the traction force magnitude maps for a single MDCK WT and E-cadherin KO cell on a soft PDMS substrate. Bottom, left and right vectorial maps of traction force for a single MDCK WT and E-cadherin KO cell on a soft PDMS substrate. B) Schematic showing the defect movement based on force balance for an extensile nematic system (left) and contractile nematic system (right) with an inset of forces exerted on neighbours by an extensile (left) and contractile (right) nematic particle. C) Schematic (left) and experimental (right) images of +1/2 defect (left, comet configuration) and −1/2 defect (right, trefoil configuration). D) Average yy- and xy-components of strain rate map around + 1/2 defect obtained from experiments (left and middle respectively) and corresponding average velocity flow field (right) for MDCK WT cells (top) (n = 912 defects from 2 independent experiments) and MDCK E-cadherin KO cells (bottom) (n = 1,884 defects from 2 independent experiments). Colour code is positive for stretching and negative for shrinkage. E) Top, phase contrast images overlaid with red lines, bottom, representative red lines, the blue spot shows the location of +1/2 and the direction of motion of this defect represented over time using an arrow obtained from experimental data for MDCK E-cadherin KO cells. These red lines represent the average local orientation of cells. Scale bars, 20μm

Figure 2| Intercellular stresses change the contractile behaviour of a 2D nematic system A) Schematic illustrating the model used in numerical simulations which incorporates cell-cell interaction through active intercellular forces, direction of cell elongation obtained from the intrinsic intracellular forces. B) Top, phase images overlaid with red lines, bottom, representative red lines, the blue spot shows the location of +1/2 and the direction of motion of this defect represented over time using an arrow obtained from simulation data for the condition without active intercellular forces. These red lines represent the average local orientation of cells. C) Average yy- and xy-components of strain rate map around + 1/2 defect obtained from simulations (left and middle respectively) and corresponding average velocity flow field (right: n = 2,083 defects) for the control condition (top) and the condition without active intercellular forces. Colour code is positive for stretching and negative for shrinkage.

Figure 3| MDCK E-cadherin KO cells show increase in cell-substrate interaction. A, B) RMS velocity (A) and the velocity correlation length normalized to the cell size (B) of the monolayer obtained from n=30 different simulations for the control condition and the condition with active intercellular forces. C) Average isotropic stress around a + 1/2 defect obtained from simulations for the control condition (left) and condition without intercellular forces (right) (n = 2,083 defects). D) Average yy (left)-, xy (middle)- and isotropic (right) components of stress around a + 1/2 defect obtained from experiments for MDCK E-cadherin KO (n = 1,428 defects). For C and D colour code, positive for tensile state, negative for compression. E, F, G) velocity correlation length (E) (n=10), velocity (F) (n=10) and mean traction force (E) (n=12) of cells within a monolayer for both MDCK WT and MDCK E-cadherin KO cells. The errors bars represent the standard deviation of this data. Unpaired t-test was performed and *$p<0.05$, **$p<0.01$, ***$p<0.001$ and ****$p<0.0001$.

Figure 4| E-cadherin removal triggers mechanotransductive changes within the monolayer. A, B) Cell spreading area (A) and aspect ratio (B) of cells within the monolayer obtained from n=2178 for MDCK WT and n=1817 for E-cadherin KO cells from 2 independent experiments. C, D, E, F) pMRLC (left), actin (right) (C), actin and paxillin (D), vinculin (E), YAP (green), and nucleus (blue) (F), staining within a monolayer for both MDCK WT and E-cadherin KO cells. C)

Western blot analysis of total MLC (bottom left) and quantification from 3 independent experiments normalized to α-tubulin. D) Area of focal adhesion (left) and length of focal adhesion within the monolayer for n=106 focal adhesions. E) Mean intensity of vinculin at the cell-cell junction (n=54). F) Distribution of YAP in nucleus, cytoplasm, or uniform distribution calculated for n=1162 (MDCK WT) and n=1008 (MDCK E-cadherin KO). G) Cell sorting observed through numerical simulation where the contractile particles (orange) are surrounded by extensile particles (green). H) Cell sorting observed when MDCK WT and MDCK E-cadherin KO cells, where WT cells are surrounded by E-cadherin KO cells (E-cadherin, green, cadherin 6, red, actin, black). XZ and YZ projection show the height difference between the two cells when mixed. Error bars represent the standard deviation. Unpaired t-test was performed and *$p<0.05$, **$p<0.01$, ***$p<0.001$ and ****$p<0.0001$. Scale bars, 20μm

Figure S1| Fibroblasts behave as a 2D contractile active nematic. A) Average yy- and xy-components of strain rate map around + 1/2 defect obtained from experiments (left and middle respectively) and corresponding average velocity flow field (right) (n = 1489 defects from 2 independent experiments) for NIH3T3 cells. Colour code is positive for stretching and negative for shrinkage. B) Average yy (left)-, xy (middle)- and isotropic (right) components of stress around a + 1/2 defect obtained from experiments for NIH3T3 (n = 1,428 defects from 2 independent experiments).

Figure S2| Characterization of MDCK E-cadherin KO cells. A) Immunofluorescence staining (top) of E-cadherin (left), β-catenin (middle) and ZO1 (right), along with a B) representative western blot and quantification for E-cadherin (left) (n=2) and β-catenin (right) (n=3). Scale bars, 20μm

Figure S3| Contractile and extensile behaviour of MCF7A cells. A) Western blot showing the reduced level of E-cadherin in siRNA generated E-cadherin KD cell line for MCF7A cells. B and C) Average velocity flow field for MCF7A control cells (n = 2047 defects from 3 independent experiments) (B) and siRNA E-cadherin KD MCF7A cells (n = 1256 defects from 3 independent experiments) (C).

Figure S4| E-cadherin removal does not affect single cell behaviour, and E-cadherin rescue changes the behaviour to a 2D extensile active nematic liquid crystal. A) Mean traction force for both MDCK WT (n=31) and MDCK E-cadherin KO cells (n=27). B) Average yy- and xy-components of strain rate map around + 1/2 defect obtained from experiments (left and middle respectively) and corresponding average velocity flow field (right) (n = 1428 defects from 2 independent experiments) for MDCK E-cadherin KO cells plated on PDMS substrates of stiffness 15kPa from which stress maps were obtained in Figure 3D. C) Average yy- and xy-components of strain rate map around + 1/2 defect obtained from experiments (left and middle respectively) and corresponding average velocity flow field (right) (n = 1767 defects from 2 independent experiments) for MDCK E-cadherin KO cells rescued with E-cadherin GFP.

Figure S5| Drug treatment changes 2D active nematic behaviour of MDCK E-cadherin KO cells. A, B, C) Average yy- and xy-components of strain rate map around + 1/2 defect obtained from experiments (left and middle respectively) and corresponding average velocity flow field (right) for MDCK E-cadherin KO cells treated with 5μM blebbistatin (A) (n = 2174 defects from 2 independent experiments), 20μM blebbistatin (B) (n = 1223 defects from 2 independent

experiments), 25µM Y27632 (C) (n = 1965 defects from 2 independent experiments). D, E) Average yy- and xy-components of strain rate map around + 1/2 defect obtained from experiments (left and middle respectively) and corresponding average velocity flow field (right) for MDCK WT cells treated with 20µM blebbistatin (D) (n = 1287 defects from 2 independent experiments), 25µM Y27632 (E) (n = 2472 defects from 2 independent experiments).

Figure S6| Substrate rigidity alters E-cadherin KO behaviour. A, B) Average yy- and xy-components of strain rate map around + 1/2 defect obtained from experiments (left and middle respectively) and corresponding average velocity flow field (right) for MDCK WT cells (A) (n = 1426 defects from 2 independent experiments) and E-cadherin KO cells (B) (n = 1041 defects from 2 independent experiments)

Figure 1

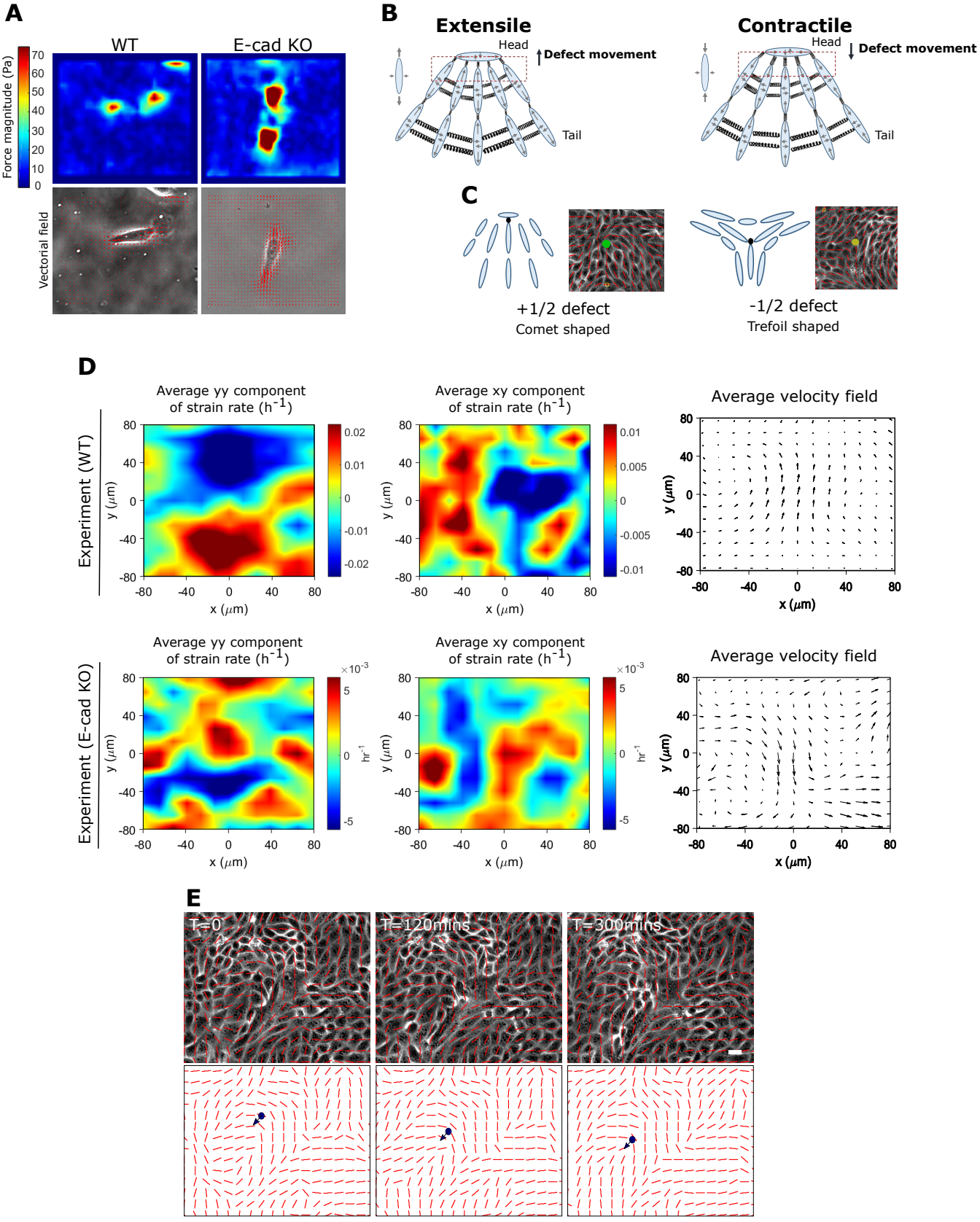
A
WT
E-cad KO
Force magnitude (Pa)
70
60
50
40
30
20
10
0
Vectorial field
B
Extensile
Head
Defect movement
Tail
Contractile
Head
Defect movement
Tail
C
+1/2 defect
Comet shaped
-1/2 defect
Trefoil shaped
D
Experiment (WT)
Average yy component of strain rate (h-1)
Average xy component of strain rate (h-1)
Average velocity field
y (μm)
x (μm)
Experiment (E-cad KO)
Average yy component of strain rate (h-1)
Average xy component of strain rate (h-1)
Average velocity field
E
T=0
T=120mins
T=300mins

Figure 2

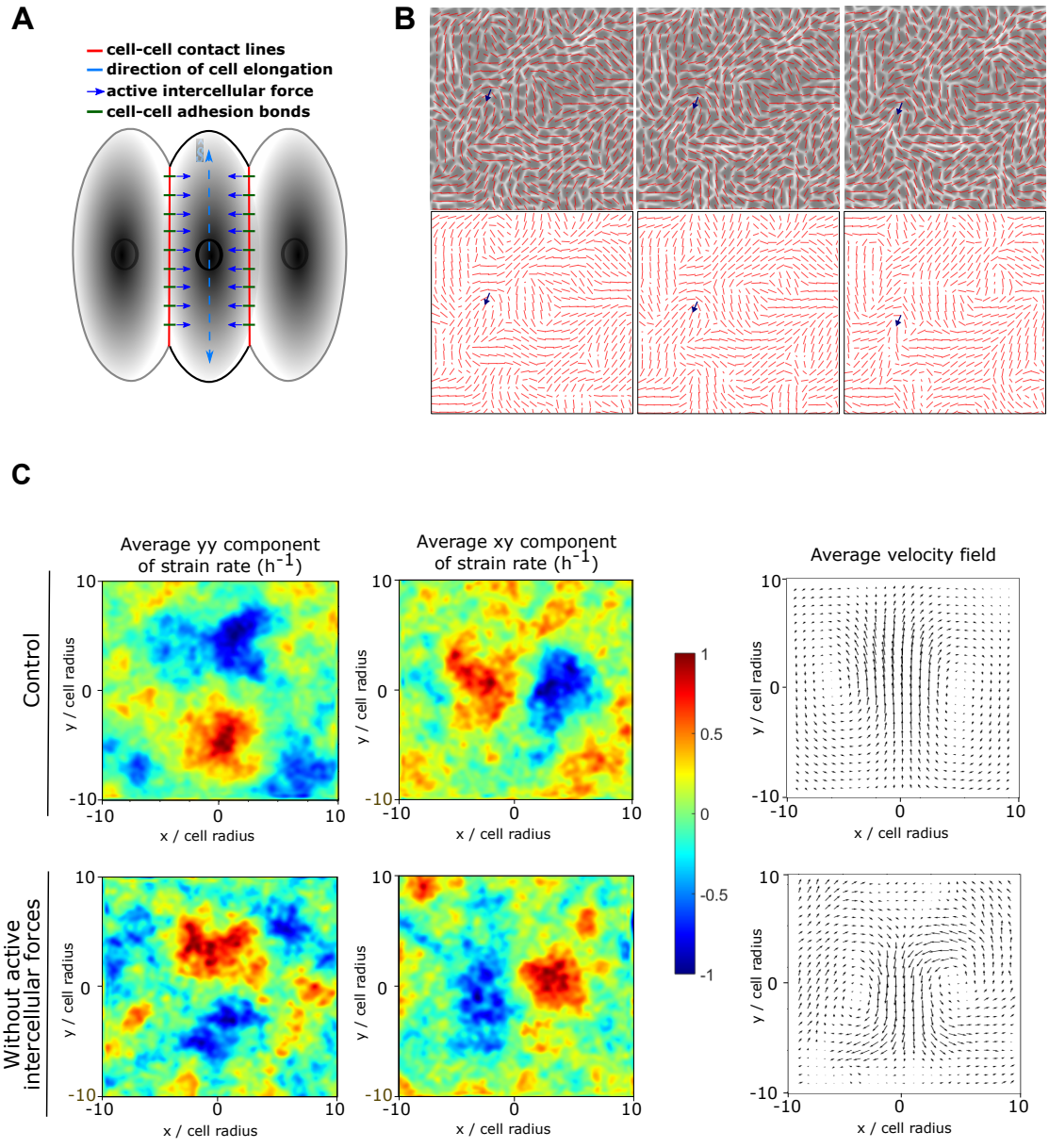
A
cell-cell contact lines
direction of cell elongation
active intercellular force
cell-cell adhesion bonds
B
C
Average yy component of strain rate (h-1)
Average xy component of strain rate (h-1)
Average velocity field
Control
Without active intercellular forces
y / cell radius
x / cell radius
10
0
-10
1
0.5
0
-0.5
-1

Figure 3

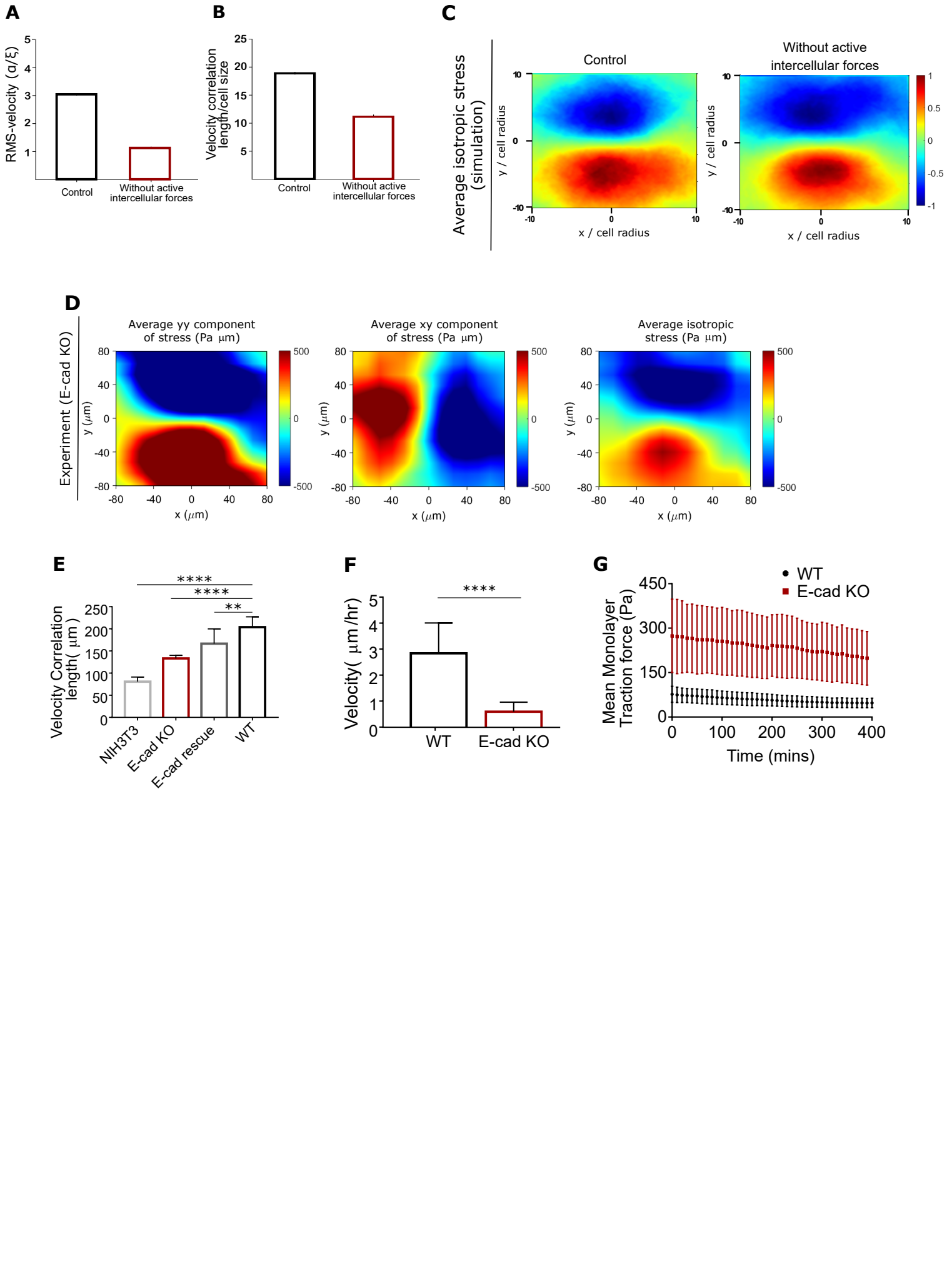
A
RMS-velocity (a/ξ)
Control
Without active intercellular forces
B
Velocity correlation length/cell size
Control
Without active intercellular forces
C
Average isotropic stress (simulation)
Control
Without active intercellular forces
y / cell radius
x / cell radius
D
Experiment (E-cad KO)
Average yy component of stress (Pa μm)
Average xy component of stress (Pa μm)
Average isotropic stress (Pa μm)
y (μm)
x (μm)
E
Velocity Correlation length(μm)
NIH3T3
E-cad KO
E-cad rescue
WT
****
****
**
F
Velocity(μm/hr)
WT
E-cad KO
****
G
Mean Monolayer Traction force (Pa)
WT
E-cad KO
Time (mins)

Figure 4

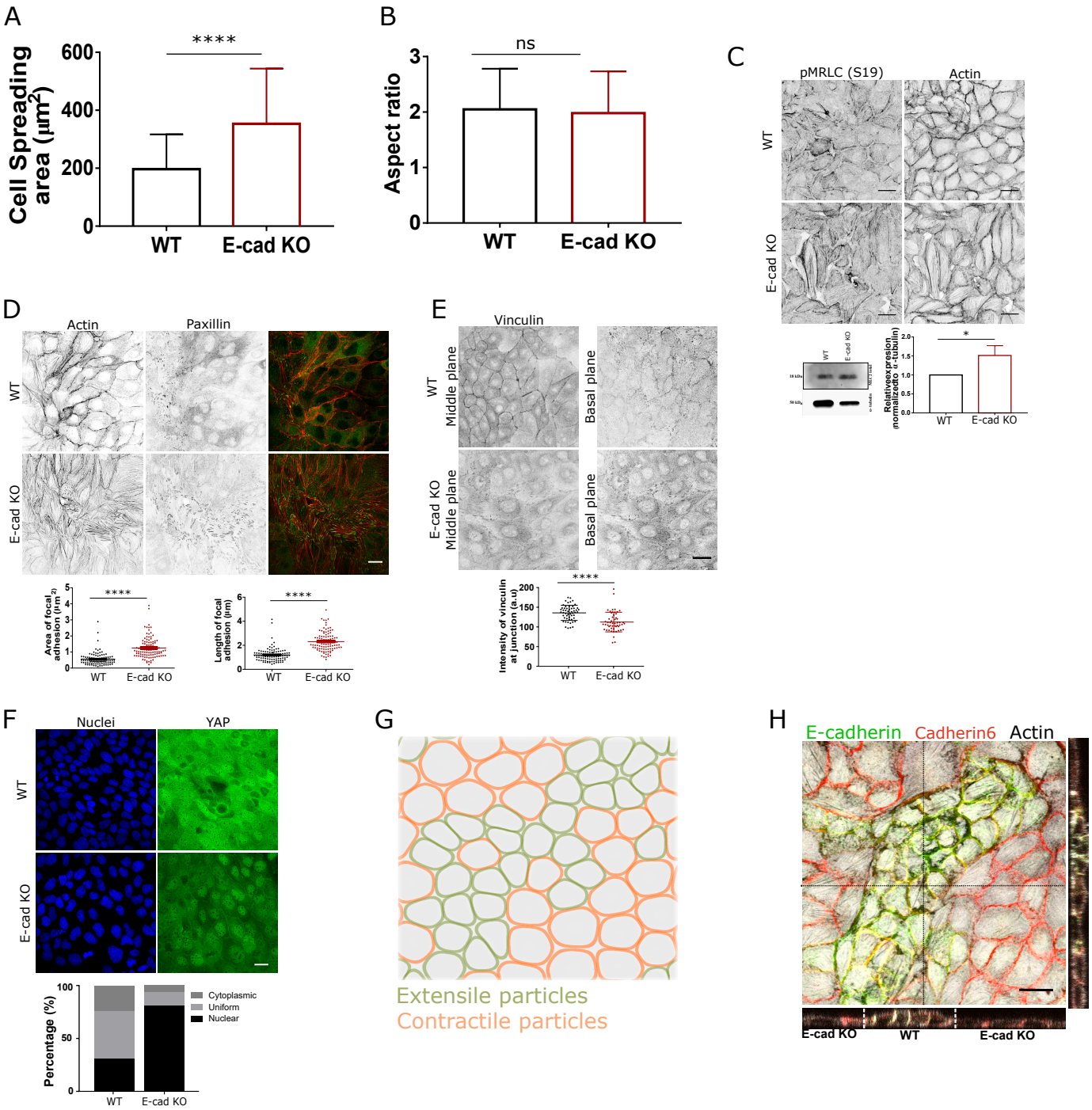
A
Cell Spreading area (µm²)
600
400
200
0
****
WT
E-cad KO
B
Aspect ratio
3
2
1
0
ns
WT
E-cad KO
C
pMRLC (S19)
Actin
WT
E-cad KO
WT
E-cad KO
Relativeexpresion (normalizedto α-tubulin)
2.0
1.5
1.0
0.5
0.0
*
WT
E-cad KO
D
Actin
Paxillin
WT
E-cad KO
Area of focal adhesion (µm²)
****
WT
E-cad KO
Length of focal adhesion (µm)
****
WT
E-cad KO
E
Vinculin
WT
Middle plane
Basal plane
E-cad KO
Middle plane
Basal plane
Intensity of vinculin at junction (a.u)
****
WT
E-cad KO
F
Nuclei
YAP
WT
E-cad KO
Percentage (%)
100
50
0
Cytoplasmic
Uniform
Nuclear
WT
E-cad KO
G
Extensile particles
Contractile particles
H
E-cadherin
Cadherin6
Actin
E-cad KO
WT
E-cad KO

Figure S1

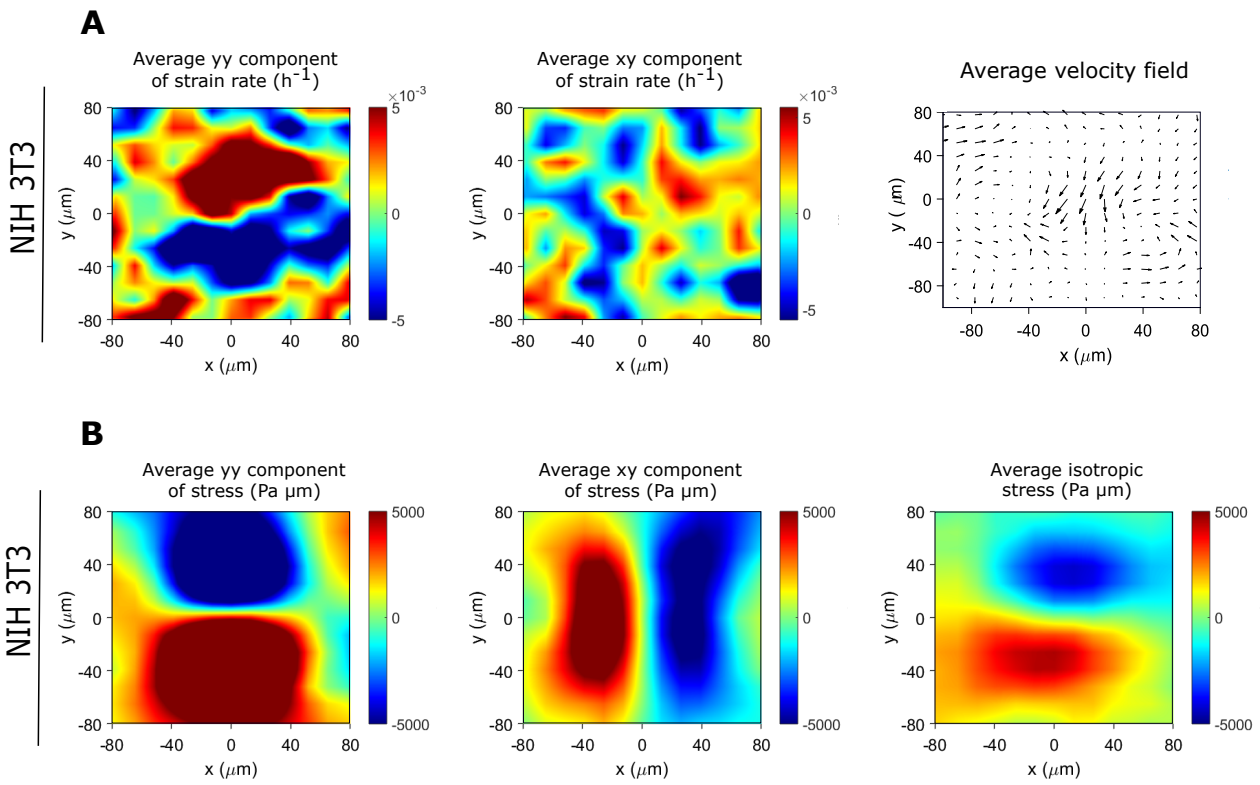
A
NIH 3T3
Average yy component of strain rate (h^{-1})
Average xy component of strain rate (h^{-1})
Average velocity field
×10^{-3}
5
0
-5
y (μm)
x (μm)
80
40
0
-40
-80
B
NIH 3T3
Average yy component of stress (Pa μm)
Average xy component of stress (Pa μm)
Average isotropic stress (Pa μm)
5000
0
-5000

Figure S2

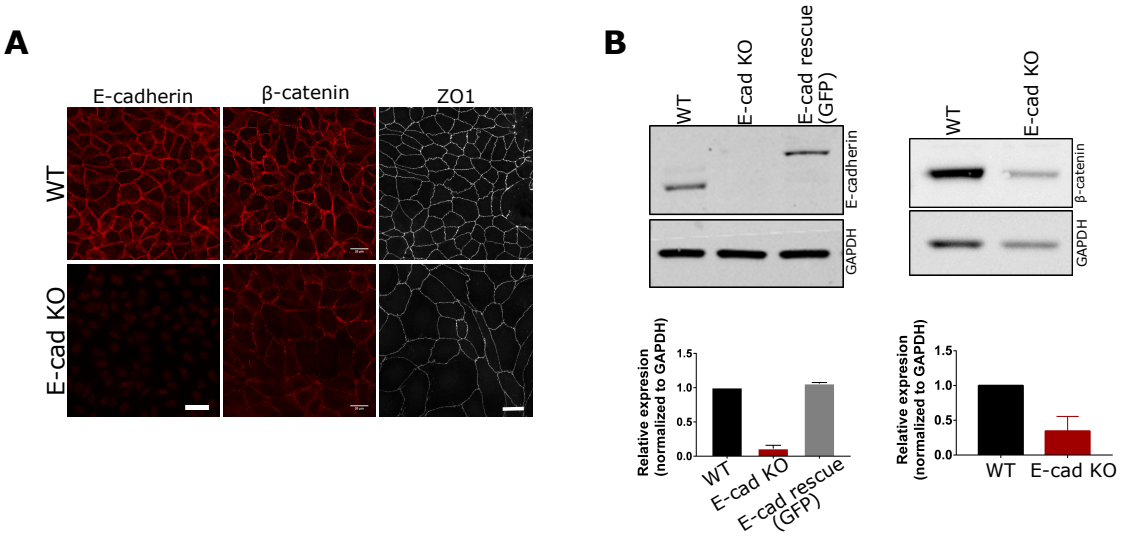
A
E-cadherin
β-catenin
ZO1
WT
E-cad KO
B
WT
E-cad KO
E-cad rescue (GFP)
E-cadherin
GAPDH
WT
E-cad KO
β-catenin
GAPDH
Relative expresion (normalized to GAPDH)
1.5
1.0
0.5
0.0
WT
E-cad KO
E-cad rescue (GFP)
Relative expresion (normalized to GAPDH)
1.5
1.0
0.5
0.0
WT
E-cad KO

Figure S3

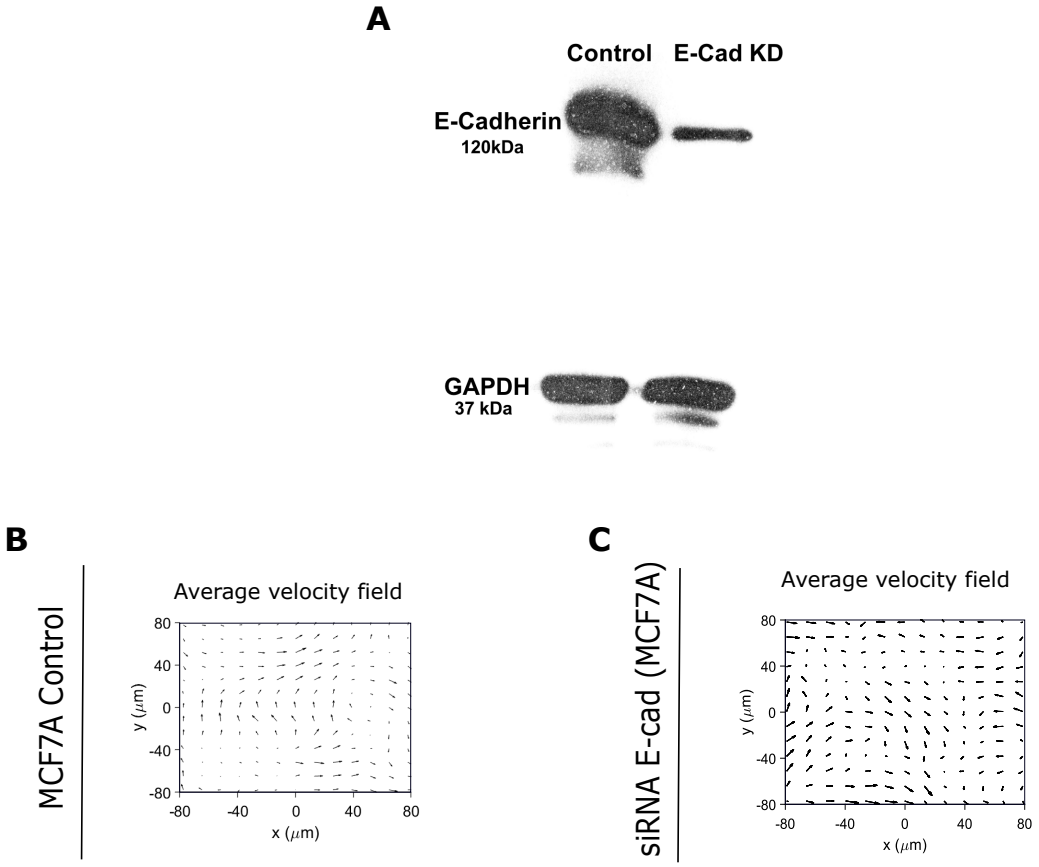
A
Control
E-Cad KD
E-Cadherin
120kDa
GAPDH
37 kDa
B
MCF7A Control
Average velocity field
y (μm)
x (μm)
C
siRNA E-cad (MCF7A)
Average velocity field
y (μm)
x (μm)

Figure S4

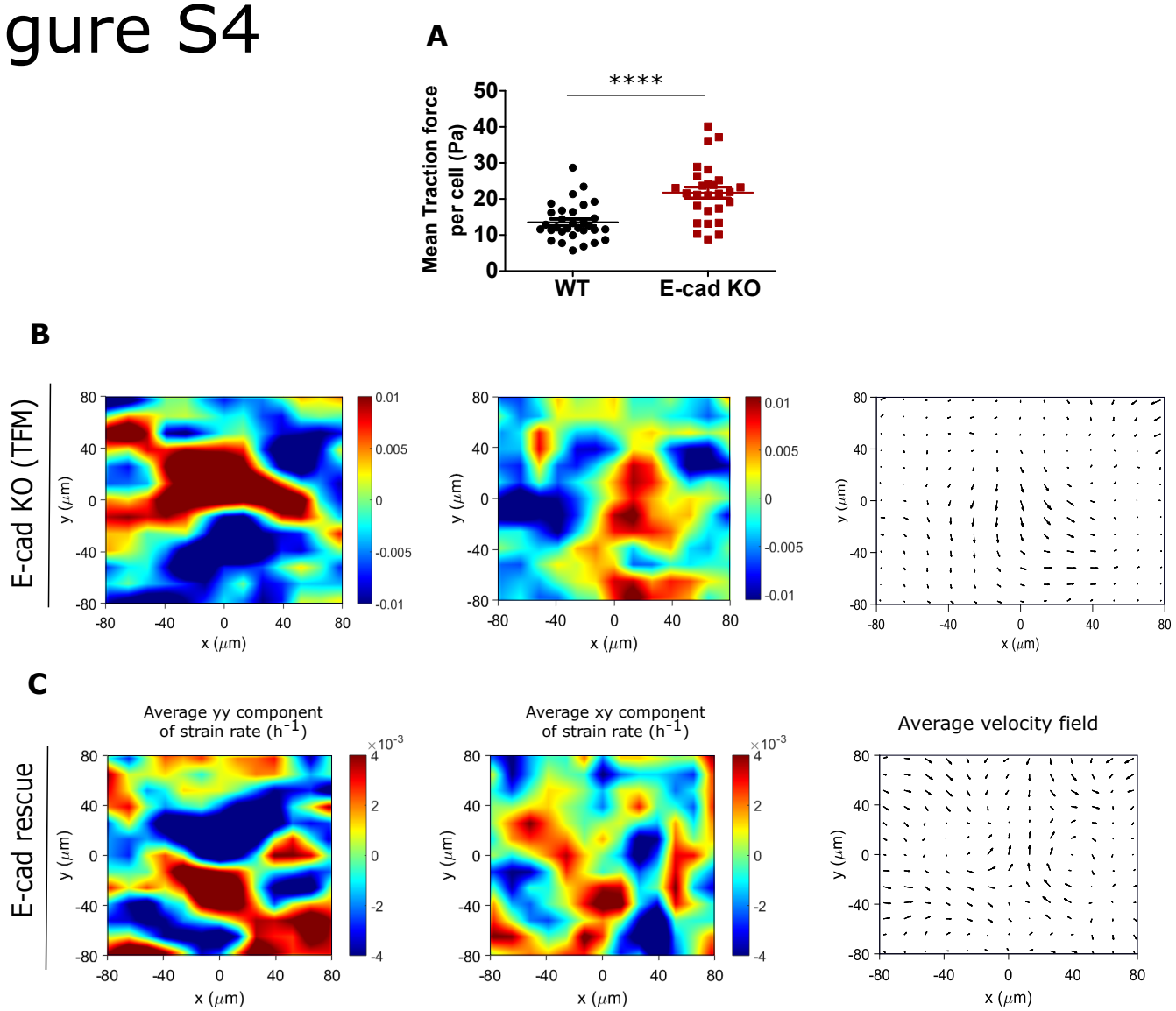
A
****
Mean Traction force per cell (Pa)
50
40
30
20
10
0
WT
E-cad KO
B
E-cad KO (TFM)
y (μm)
x (μm)
0.01
0.005
0
-0.005
-0.01
C
E-cad rescue
Average yy component of strain rate (h^{-1})
Average xy component of strain rate (h^{-1})
Average velocity field
×10^{-3}
4
2
0
-2
-4
80
40
0
-40
-80

Figure S5

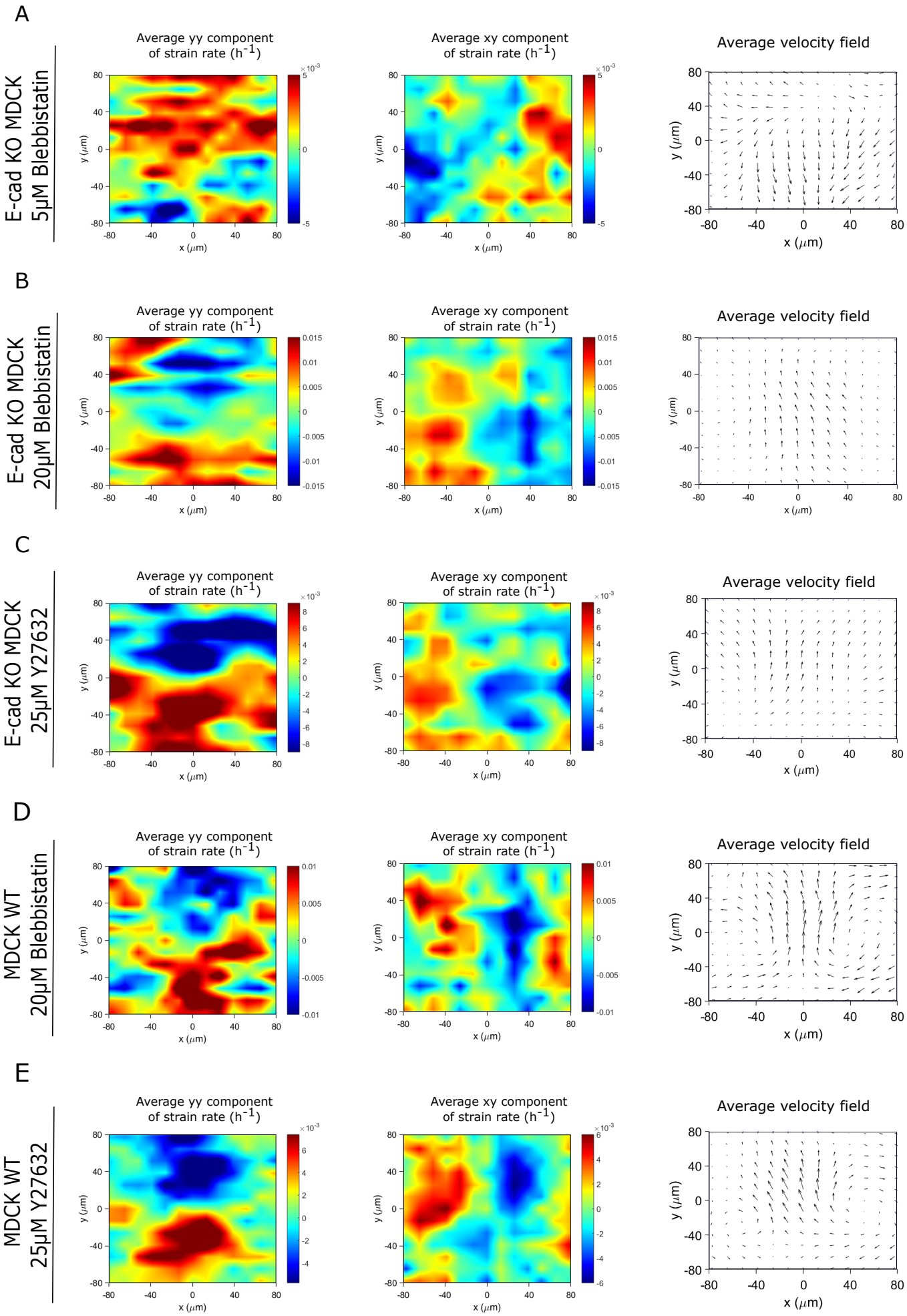
A
E-cad KO MDCK
5μM Blebbistatin
Average yy component of strain rate (h^{-1})
Average xy component of strain rate (h^{-1})
Average velocity field
B
E-cad KO MDCK
20μM Blebbistatin
C
E-cad KO MDCK
25μM Y27632
D
MDCK WT
20μM Blebbistatin
E
MDCK WT
25μM Y27632
x (μm)
y (μm)

Figure S6

A

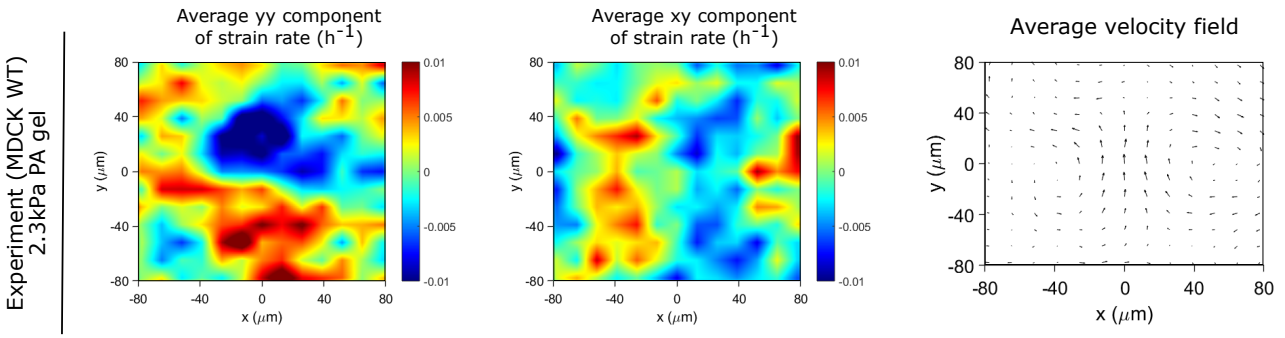
Experiment (MDCK WT)
2.3kPa PA gel
Average yy component
of strain rate (h-1)
Average xy component
of strain rate (h-1)
Average velocity field
y (μm)
x (μm)
80
40
0
-40
-80
0.01
0.005
0
-0.005
-0.01

B

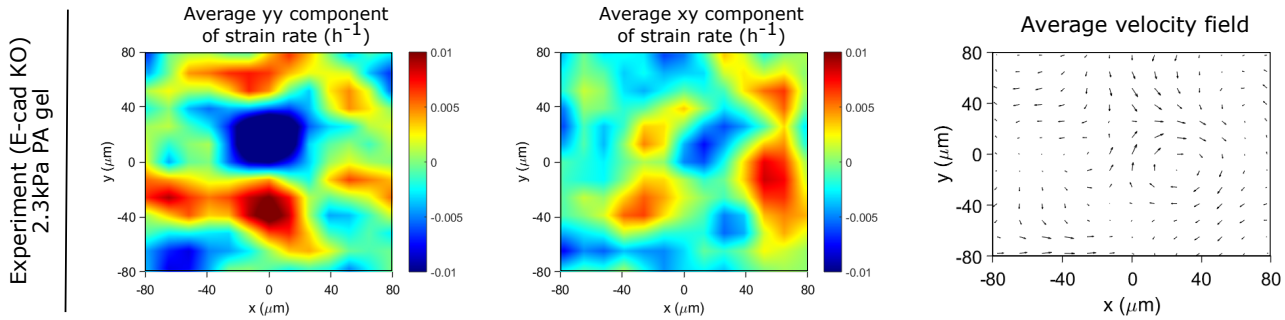
Experiment (E-cad KO)
2.3kPa PA gel
Average yy component
of strain rate (h-1)
Average xy component
of strain rate (h-1)
Average velocity field
y (μm)
x (μm)
80
40
0
-40
-80
0.01
0.005
0
-0.005
-0.01

Drug	Pathway affected	MDCK WT	MDCK E-cadherin KO
No drug	--	Extensile	Contractile
Blebbistatin (5 µM)	Non-muscle Myosin II	--	Contractile
Blebbistatin (20 µM)	Non-muscle Myosin II	Extensile	Extensile
Y27632 (25 µM)	ROCK 1 and 2	Extensile	Extensile